Tectonophysics 789 (2020) 228532

Contents lists available at ScienceDirect

Tectonophysics

journal homepage: www.elsevier.com/locate/tecto

Significance of crustal extension and magmatism to gold deposits beneath Jiaodong Peninsula, eastern North China Craton: Seismic evidence from receiver function imaging with a dense array

Guiping Yu[a,d], Tao Xu[a,e,*], Yinshuang Ai[b,e], Ling Chen[a,d,e], Jinhui Yang[a,c]

[a] State Key Laboratory of Lithospheric Evolution, Institute of Geology and Geophysics, Chinese Academy of Sciences, Beijing 100029, China
[b] Key Laboratory of Earth and Planetary Physics, Chinese Academy of Sciences, Beijing 100029, China
[c] Innovation Academy for Earth Science, CAS, Beijing 100029, China
[d] University of Chinese Academy of Science, Beijing 100049, China
[e] CAS Center for Excellence in Tibetan Plateau Earth Sciences, Beijing 100101, China

ARTICLE INFO

Keywords:
Jiaodong Peninsula
Gold deposits
Crustal extension
Dense array
Receiver function

ABSTRACT

The Jiaodong Peninsula, located in the eastern North China Craton (NCC), is a key region to study the genetic linkage between large-scale gold mineralization and craton destruction. We construct a fine crustal structural image across the Jiaodong Peninsula, using teleseismic P-wave receiver function data recorded by a dense linear array of 340 short-period seismic stations. The results reveal significant similarities and differences between the eastern and the western Jiaodong Peninsula. The presence of an intracrustal low-velocity zone, and the north-dipping interfaces beneath the Jiaolai Basin imply widespread crustal extension in the whole region. In the northwest Jiaodong metallogenic belt, the identified detachment faults, small vertical velocity gradients in the upper part of the lower crust and the thick crust-mantle transition zone provide evidences for intense crustal extension in this area, probably coeval with the peak of lithospheric thinning and destruction of the eastern NCC in the Late Mesozoic. In the Muru metallogenic belt, distinct differences are found on the opposite sides of the Wulian-Yantai Fault Zone (WYFZ), in the depth and structure of the Moho, intracrustal low-velocity zone, upper crustal Vp/Vs ratios, and Bouguer gravity anomalies, indicating that the WYFZ may be a steep transcrustal fault. We propose that the coupled effects of intense crustal extension, voluminous magmatism and water released from the subducting Paleo-Pacific slab may have been responsible for the concentrated gold deposits in the northwest Jiaodong during the peak of the NCC destruction, while limited gold deposits in the Muru metallogenic belt may have been attributed to relatively weak crustal extension and steep faults.

1. Introduction

The eastern North China Craton (NCC) is not only the most typical example of ancient craton destruction in the world (Carlson et al., 2005; Wu et al., 2008), but also the most important gold province in China (Fan et al., 2003; Yang et al., 2003a; Song et al., 2015). Massive gold deposits are generally concentrated along the margin of eastern NCC, and they were mainly formed in the Early Cretaceous (130– 120 Ma) (Yang et al., 2003a), probably coeval with the peak of craton destruction (~125 Ma) (Wu et al., 2005; Xu et al., 2009; Zhu and Zheng, 2009; Zhu et al., 2011). The temporal and spatial coincidence between the large-scale gold mineralization and the craton destruction imply that there exists a genetic linkage between them. Many petrological, geological and geochemical investigations have shown that extensional structure and mantle derived magmatism, the important manifestations of craton destruction, may also be the key ore-controlling factors of gold deposits in the eastern NCC (Shen et al., 2005; Mao et al., 2008; Goldfarb and Santosh, 2014; Zhu et al., 2015, 2017), which are significantly different from the orogenic gold deposits (Groves et al., 1998; Goldfarb et al., 2001). However, the specific linkage between the gold mineralization and the intense tectonic-magmatic activities is still controversial. The Jiaodong Peninsula, located in the eastern margin of the NCC, is the largest gold concentration area in China (Qiu et al., 2002; Fan et al., 2003; Yang et al., 2003a), and the distribution of its gold deposits is very uneven (Yang et al., 2014; Li et al., 2015; Song, 2015), which is a great matter of concern. Thus, the Jiaodong Peninsula

* Corresponding author at: State Key Laboratory of Lithospheric Evolution, Institute of Geology and Geophysics, Chinese Academy of Sciences, Beijing 100029, China.
E-mail address: xutao@mail.iggcas.ac.cn (T. Xu).

https://doi.org/10.1016/j.tecto.2020.228532
Received 1 February 2020; Received in revised form 5 June 2020; Accepted 8 June 2020
Available online 10 June 2020

is one of the best places to study the above crucial issue. A high-resolution seismic image of the crustal structure and a comparative study of different metallogenic belts are required to analyze the causes of regional metallogenic differences, and to reveal the linkage between the gold mineralization and the intense tectonic-magmatic activities.

In recent years, many geophysical investigations (Ma et al., 1991; Yang, 2002; Chen et al., 2006; Zheng et al., 2008b; Jia et al., 2014; Pan et al., 2015; Li et al., 2018; Yu et al., 2018; Zhang et al., 2018; Meng et al., 2019) have been carried out in the Jiaodong Peninsula and its adjacent areas, providing direct imaging results of crust-mantle structure for studying the regional tectonic background and the deep dynamic process. Unfortunately, high-resolution seismic observations across main gold concentration areas have been scarce. The limited researches using deep seismic reflection (Yang, 2002) and receiver function imaging (Chen et al., 2006; Zheng et al., 2008b) so far focus only on the Sulu orogenic belt and the Tanlu Fault Zone area, respectively. Surface wave tomography (Li et al., 2018) can cover the entire Jiaodong Peninsula, but suffer from poor lateral resolution due to the limited data coverage. Only deep seismic sounding (Pan et al., 2015) and magnetotelluric sounding (Zhang et al., 2018) have provided medium-resolution crustal imaging results across the Jiaodong Peninsula, while shallow reflection seismic exploration with the high-resolution (Yu et al., 2018) usually is just arranged in the inner part of the gold concentration area due to its high cost. The receiver function imaging method based on short-period seismic arrays is a new technology developed in recent years (Šumanovac et al., 2016; Liu et al., 2017). It combines the portability of short-period seismometers and the high-resolution feature of receiver function method, making the layout of dense stations and therefore the high-resolution crustal structure imaging become easier.

In this study, based on the data of a short-period dense linear seismic array across the Jiaodong Peninsula, we construct a high-resolution crustal structure image using teleseismic P-wave receiver function method (Langston, 1979), and compare our new results with the previous geophysical studies, Bouguer gravity anomalies and surface geology. Through the analysis of multiple phases, we have particularly identified an intracrustal low-velocity zone (LVZ) and the lateral variations of the Moho. On the basis of our imaging results, we discuss the crustal structure differences between the northwest Jiaodong metallogenic belt and the Muru metallogenic belt, the possible influence of the structural differences on the regional metallogenic differences, and the dynamic mechanism of the massive gold deposits and the craton destruction.

2. Geologic setting

The Jiaodong Peninsula is located in the eastern margin of the NCC and the east of Tanlu Fault Zone. It is mainly composed of three tectonic units, including Jiaobei uplift, Sulu orogenic belt and Jiaolai basin (Fig. 1). The Jiaobei uplift and the Sulu orogenic belt are bounded by the Wulian-Yantai Fault Zone (WYFZ), and are welded by the Jiaolai basin in their central section (Li et al., 2007, 2012). As the largest gold concentration area in China, the Jiaodong Peninsula develops endogenetic hydrothermal gold deposits, and the ore-host rocks are mainly Archean metamorphic rocks and Mesozoic granitic rocks, with widespread development of Mesozoic tectonics and magma (Qiu et al., 2002; Fan et al., 2003; Yang et al., 2003a; Mao et al., 2008; Deng et al., 2014; Li et al., 2015; Song et al., 2015; Wen et al., 2015; Yang and Santosh, 2015). The massive gold mineralization and complex crustal structure in the Jiaodong Peninsula are closely related to the processes of two important geological events since the Mesozoic, including the Yanshanian strong tectonic-magmatic activities and the Indosinian continental collision.

In the Triassic, the South China Block subducted northward under the NCC. After the continental collision and the exhumation of ultra-high pressure metamorphic (UHPM) rocks, the Sulu UHPM belt and synorogenic granites were formed (Li et al., 1993; Yin and Nie, 1993; Zhang, 1997; Zhao et al., 2017). Geologists and geophysicists generally consider that the WYFZ in the north of the Sulu orogenic belt is a strongly modified Triassic collision suture (Okay and Sengor, 1992; Gilder et al., 1999; Yang, 2002; Tang et al., 2007; Zhou et al., 2008), although there are still some controversies (Li, 1994; Faure et al., 2001; Zheng et al., 2005). The WYFZ is a brittle strike-slip fault zone observed from the surface, and undergone a left strike-slip compression transition in the Late Jurassic, an extension transition in the early Cretaceous, and a right strike-slip stretch transition in the Paleogene (Zhai et al., 2000; Zhang et al., 2007). It can be further divided into the Wulian-Qingdao Fault Zone in the west and the Muping-Jimo Fault Zone in the east. The latter concretely is composed of the Taocun fault, the Guocheng fault, the Muping fault and the Haiyang fault. The WYFZ referred to in this paper mainly is the Muping fault.

In the Late Mesozoic, mainly affected by the westward subduction of the Paleo-Pacific plate (Izanagi plate) (Woods and Davies, 1982; Seton et al., 2012), large-scale destruction occurred in the eastern NCC (Xu et al., 2009; Zhu and Zheng, 2009; Zhu et al., 2011). The evidences of craton destruction in the Jiaodong Peninsula mainly include: (1) strong crustal and lithospheric thinning (Zheng et al., 2006, 2008b; Chen et al., 2006, 2008, 2009; Chen, 2010); (2) various types of extensional tectonics developing, such as the Jiaolai faulted basin, the Linglong metamorphic core complex (MCC) in the Jiaobei uplift, and the Tanlu Fault Zone (Gilder et al., 1999; Zhang et al., 2003; Li et al., 2007; Lin and Wei, 2018; Zhu et al., 2018); (3) large-scale granitic emplacement and extensive volcanic eruptions (Liu et al., 2005; Yang et al., 2005; Zhang and Zhang, 2007).

Geological, petrological and geochemical investigations have shown that there are significant differences in the types, scales and ore-controlling structures of gold deposits in the east and the west of the Jiaodong Peninsula (Yang et al., 2014; Li et al., 2015; Song, 2015). The extremely uneven distribution of gold deposits has always been a great concern. For example, the gold reserves in the northwest Jiaodong metallogenic belt (Jiaobei uplift) are highly concentrated (accounting for 3/4 of the total reserves in the Jiaodong Peninsula), while reserves in the Muru metallogenic belt (the junction of the Sulu orogenic belt and the Jiaolai basin) are rare. The northwest Jiaodong metallogenic belt mainly develops large-scale fracture-altered style gold deposits, which are controlled by NE-NNE trending gently inclined detachment faults, represented by the Sanshandao fault, the Jiaojia fault and the Zhaoping fault. The Muru metallogenic belt mainly develops quartz vein type gold deposits, which are controlled by steep faults such as the WYFZ and the Jinniushan fault.

3. Data and method

From March to April in 2017, a NWW-SEE-trending dense linear seismic array was emplaced in the Jiaodong Peninsula (red inverted triangles in Fig. 1b), across the Jiaobei uplift, the Jiaolai basin and the Sulu orogenic belt. The array consists of 340 short-period seismic stations, with an average interstation spacing of 500 m. Seismometers with a frequency range of 2.5– 150 Hz were used. Three-component seismograms were selected from 25 well-recorded events with magnitudes ≥ 5.0 and epicentral distances between 30° and 90°. Firstly, waveforms were windowed from 20 s before to 100 s after the P-wave first arrival, and then were rotated from a vertical-north-east (ZNE) coordinate system to a vertical-radial-transverse (ZRT) coordinate system after band-pass filtering between 0.05 and 5 Hz. Finally, the iterative time-domain deconvolution approach (Ligorría and Ammon, 1999) was used to calculate the P-wave radial receiver functions for further processing. A Gaussian parameter of 5 was adopted in the deconvolution. In addition, data (from January 2017 to November 2018) of several permanent broadband seismic stations (black triangles in Fig. 1b) were used for auxiliary imaging to analyze specific structural features.

Considering the uneven distribution of earthquake events (inset in

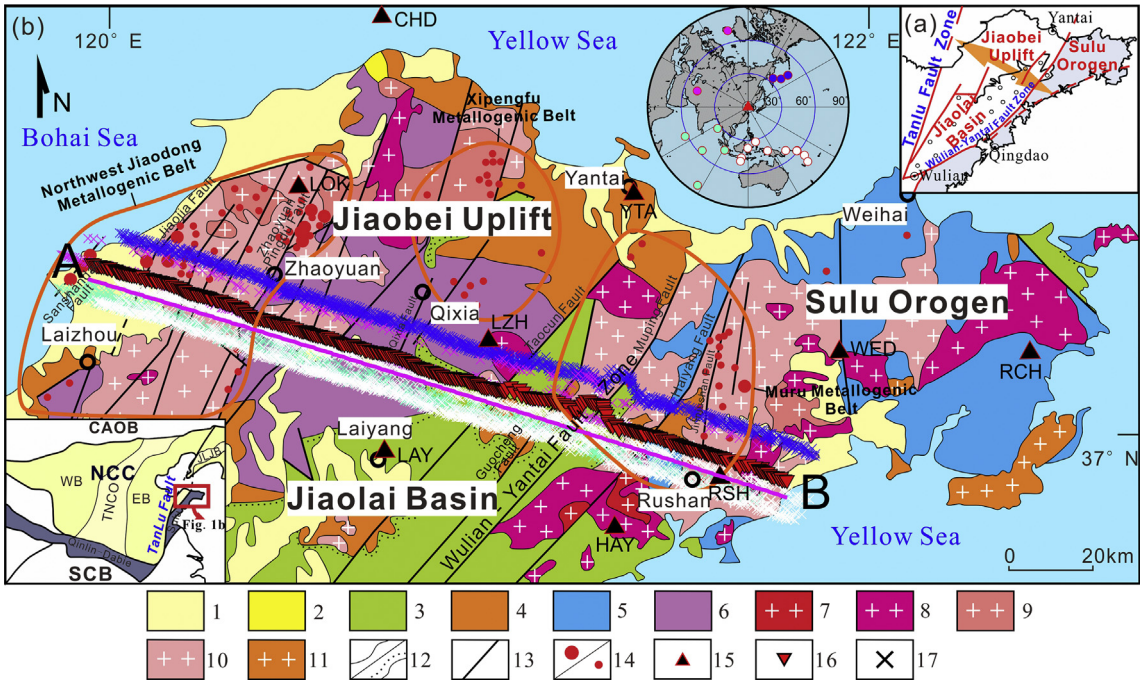

Fig. 1. Regional geological map. (a) Simplified tectonic map of the Jiaodong Peninsula. Orange arrows show the extension direction of lithosphere in the Late Mesozoic. (b) Geological map of the investigation area (modified from Song et al., 2015) and distribution of stations. 1, Quaternary loose sediments; 2, Paleogene-Neogene terrestrial volcanic-sedimentary strata; 3, Cretaceous continental volcanic-sedimentary strata; 4, Paleoproterozoic-Neoproterozoic shore-shallow marine facies strata; 5, Neoproterozoic with eclogite granitic gneiss; 6, Archean granite-greenstone belt; 7, Cretaceous Laoshan granite; 8, Cretaceous Weideshan Granite; 9, Cretaceous Guojialing granodiorite; 10, Jurassic granite; 11, Triassic granitoids; 12, conformity/ unconformity; 13, fault; 14, large to super-large gold deposit/ medium gold deposit; 15, broadband seismic station; 16, short-period seismic station; 17, piercing points of rays at 33 km depth (reference model: Vp = 6.3 km/s, Vp/Vs = 1.76). The total 25 earthquake events are plotted on the top, in which white circles denote the 12 events in southeast direction. Pink solid line AB denotes the position of CCP stacking profile. The bottom inset shows the tectonic setting of the study region in eastern China. CAOB, Central Asian orogenic belt; NCC, North China Craton; SCB, South China Block; WB, Western Block; EB, Eastern Block; TNCO, Trans-North China Orogen; JLJB, Jiao-Liao-Ji Belt. (For interpretation of the references to colour in this figure legend, the reader is referred to the web version of this article.)

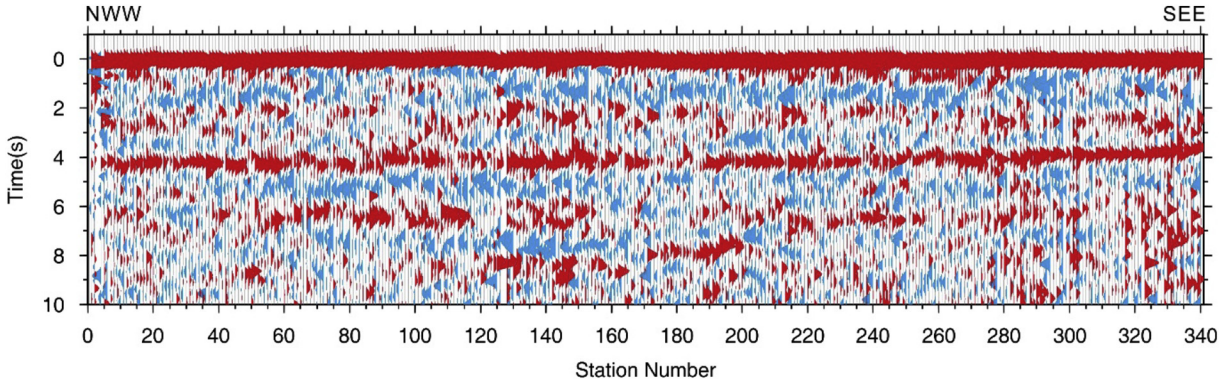

Fig. 2. Stacked P-wave receiver functions for all 340 stations along the profile. Only data of 12 events from the southeast back azimuth is used. Receiver functions (Gauss 5.0) are stacked after moveout correction (Yuan et al., 1997) based on IASP91 velocity model (Kennett and Engdahl, 1991) with a reference horizontal slowness p = 6.4 s/deg.

Fig. 1b), we chose the southeast back azimuth (120° ~ 210°) as the dominant back azimuth (12 events with high signal-to-noise ratios are concentrated there), which is nearly perpendicular to the main tectonic strike (NE-NNE; Yang et al., 2003a). This means that teleseismic rays are nearly along the linear seismic array and the corresponding receiver functions can directly reflect the crustal structure beneath the survey line. After careful visual inspection, a total number of 1056 receiver functions from the southeast back azimuth were selected. Fig. 2 shows the stacking receiver function waveforms of each station after moveout correction with a reference horizontal slowness p = 6.4 s/deg. Ps converted phases from the Moho are clearly detected at around ~4 s. Based on the above data, we further carried out H-κ stacking (Fig. 3b and d), common conversion point (CCP) stacking imaging (Fig. 3b, Fig. 7) and S-wave velocity inversion (Fig. 8).

It should be noted that CCP stacking imaging of Ps phase (Fig. 3b) and multiple phases (Fig. 7) used receiver functions of a Gaussian parameter of 5 (frequency band 0.01– 2.4 Hz) and 2.5 (frequency band 0.01– 1.2 Hz), respectively. An enlarged version of multiple phase images (Fig. S5) using high frequency data (a Gaussian parameter of 5) is provided in the supplementary materials. We have compared the imaging results in different frequency bands (Fig. S1) and find that the main features are robust. The difference is that the multiple phases of the main velocity discontinuities are relatively narrow while using high frequency data (Fig. S5).

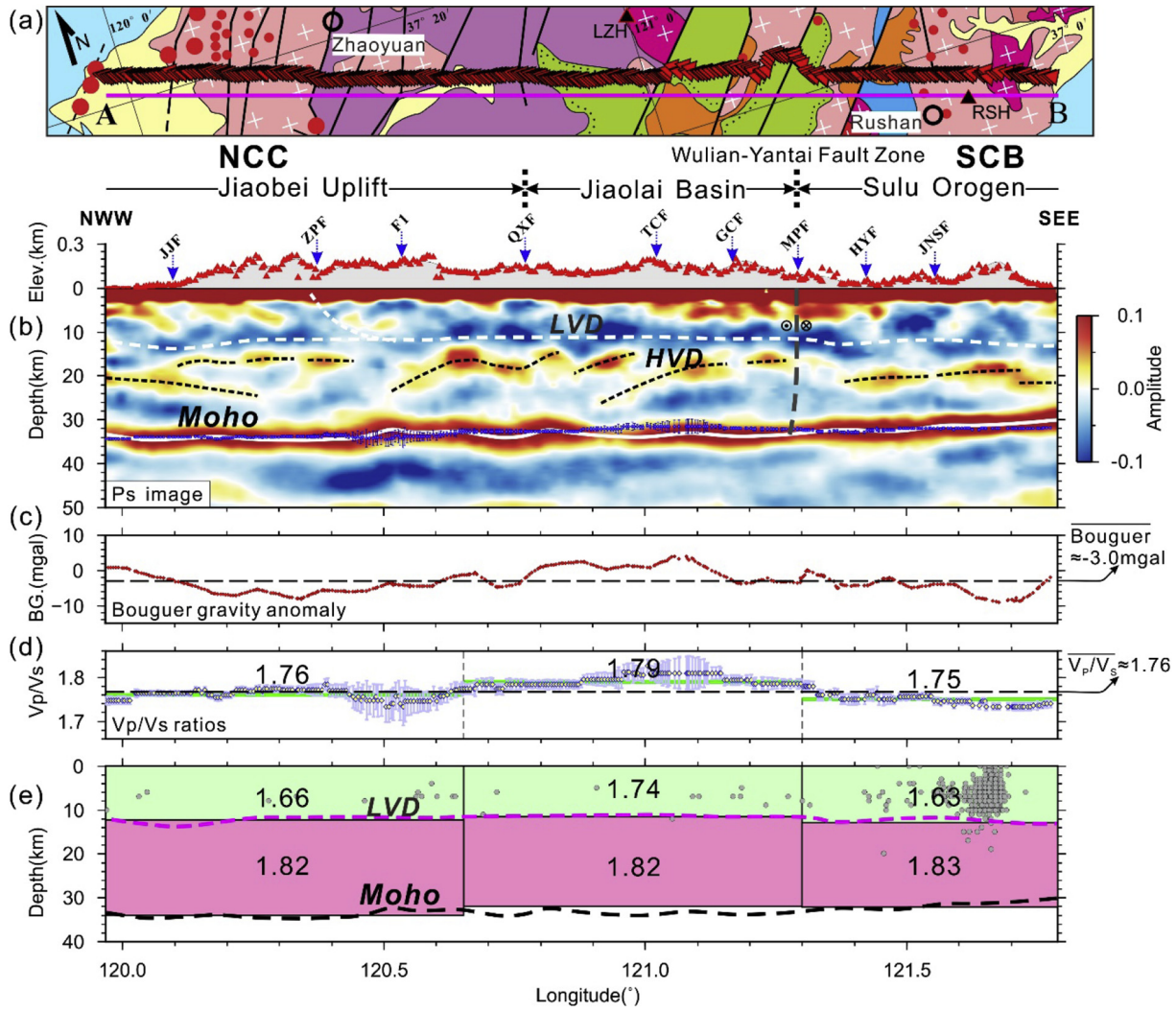

Fig. 3. Receiver function imaging of the crust. (a) Simplified geology map along the survey line. (b) CCP image of Ps phase (0.01– 2.4 Hz). White solid line, white dotted line, and black dotted line denote Moho, LVD and HVD, respectively; blue circle denotes the crustal thickness from H-κ stacking. (c) Bouguer gravity anomalies based on a global Earth gravitational model (EGM2008). (d) Crustal Vp/Vs ratios of each station (yellow diamond). The weights of Ps, PpPs, and PpPs + PpSs phases for H-κ stacking are 0.5, 0.2 and 0.3, rcespectively. Green solid line denotes the average of each tectonic unit; the black dotted line denotes the regional average. (e) Vp/Vs ratios and thicknesses of upper and lower crust. Gray circles are the projection of the historical earthquakes (2000– 2018) within 10 km of the survey line. Above images are only based on the 12 events of the southeast back azimuth (120° ~ 210°). JJF, Jiaojia fault; ZPF, Zhaoyuan-Pingdu fault; QXF, Qixia fault; TCF, Taocun fault; GCF, Guocheng fault; MPF, Muping fault; HYF, Haiyang fault; JNSF, Jinniushan fault. (For interpretation of the references to colour in this figure legend, the reader is referred to the web version of this article.)

In fact, events from the northeast back azimuth (30° ~ 60°) also have high signal-to-noise ratios. However, due to their ray paths are along the main tectonic strike, multiple phases of the crystalline basement are too strong, making it difficult to identify intracrustal velocity discontinuities (Fig. S2). Therefore, the events of northeast back azimuth are only used for H-κ stacking (Fig. 4) and longitudinal CCP imaging (Fig. 5) to analyze the Moho variations on the opposite sides of the WYFZ. Usually, because the average interstation spacing is tens of kilometers, position difference of piercing points between teleseismic rays from different back azimuths can be ignored, and different events are used together for H-κ stacking. However, this paper adopts a dense array with an interstation spacing of only 500 m. As we know, the Ps conversion/piercing point of a teleseismic ray at Moho depth (~33 km) is about 10 km away from the station (Fig. 1). For two teleseismic rays from opposite directions, the distance between their primary phases' piercing points can reach about 20 km. The distance between their multiple phases' piercing points is greater. Therefore, the back azimuths of different events must be considered and the high-resolution of the dense array can be kept well by only using the data of a certain back azimuth. In this study, the events of the southeast back azimuth and the northeast azimuth are used for H-κ stacking separately. The two group of results can reflect the crustal thicknesses of the both sides of the survey line, respectively. Due to the lack of high-resolution 3D Vp models, an average bulk Vp (6.3 km/s) extracted from the deep seismic sounding profile (Pan et al., 2015) was used for H-κ stacking. The Vp at different positions fluctuates within 0.1 km/s compared with the average value. According to the empirical formula of Zhu and Kanamori (2000), we can estimate that the error of the crustal thicknesses caused by the uncertainty of Vp is within 0.5 km. The stacking weight of each seismic phase is determined by referring to the development of multiple phases of all stations (Fig. S4). For the southeast back azimuth (120°-210°), the weights of Ps, PpPs and PpSs + PsPs are 0.5, 0.2 and 0.3, respectively. For the northeast back azimuth (30°-60°), the weights of Ps, PpPs and PpSs + PsPs are 0.5, 0.4 and 0.1, respectively.

The events with high signal-to-noise ratios are limited in this study. We have tried to use teleseismic PP phase to calculate the receiver function as a supplement, but the results of intracrustal phases are not very ideal compared with that of direct P phase. Fortunately, the

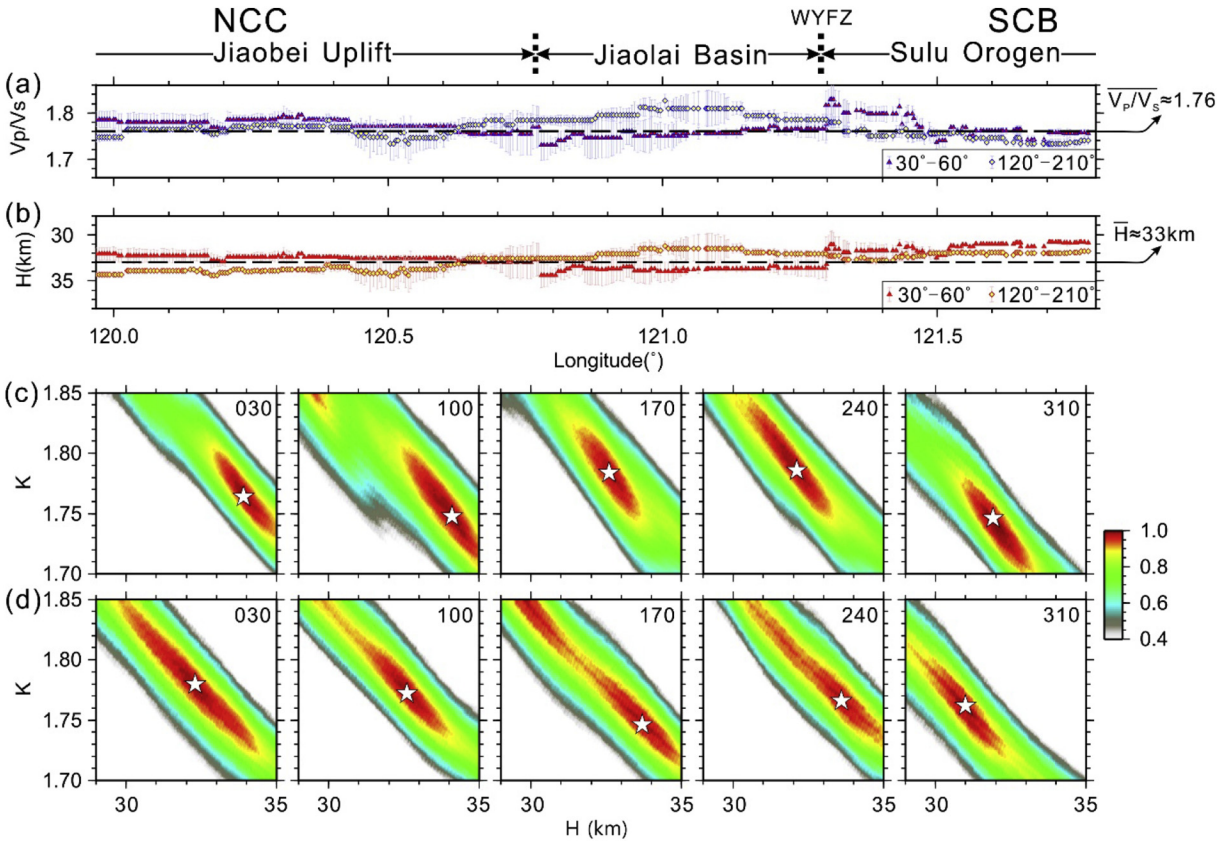

Fig. 4. H-κ stacking results based on events of two different back azimuths. (a) and (b) show the Vp/Vs ratio and crustal thickness results based on H-κ stacking (Vp = 6.3 km/s), respectively. Diamond denotes the result of the southeast back azimuth (120°-210°), and the weights of Ps, PpPs and PpSs + PsPs are 0.5, 0.2 and 0.3, respectively. Triangle denotes the result of the northeast back azimuth (30°-60°), and the weights of Ps, PpPs and PpSs + PsPs are 0.5, 0.4 and 0.1, respectively. (c) and (d) are the H-κ scanning results of the southeast back azimuth (120°-210°) and the northeast back azimuth (30°-60°), respectively. Five stations are shown as examples, including 030, 100, 170, 240 and 310.

similarity between the receiver functions of the short-period seismic stations (Fig. 2) and that of the broadband permanent stations (Fig. S6) indicate that the main features (including the negative phase at ~1.5 s, the positive phase at ~2 s, and the Moho phase at ~4 s) are robust. In addition, although receiver functions with high signal-to-noise ratios are limited, dense seismic stations still can ensure that there is enough data in each bin for CCP stacking. According to the setting of parameters in this study, the width (parallel to the profile) of the CCP stacking bin is about 10 km at the depth of 33 km. In other words, receiver functions of about 20 adjacent stations are stacked in one stacking bin. Such a smooth scale can give consideration to both high resolution and high signal-to-noise ratio. As for the H-κ stacking, to obtain stable results based on the limited events, we reduced the lateral resolution appropriately by using the stacking result of all receiver functions of 61 adjacent stations as the result of central station.

4. Seismic imaging results

4.1. Lateral variations of Moho depth

H-κ stacking of receiver function is an effective technique to estimate the crustal thickness and the average Vp/Vs ratio under each station (Zhu and Kanamori, 2000). The H-κ stacking results of the southeast back azimuth events (blue circles in Fig. 3b) show that average crustal thickness in the Jiaodong Peninsula is about 33 km, and there is a thinning trend from northwest to southeast as a whole, basically consistent with the results of deep seismic sounding (Pan et al., 2015). Interestingly, it seems that there is a dislocation of the Moho on the opposite sides of the WYFZ. However, the lateral variation is small and it may also be caused by data errors. For better identification, we further provide the H-κ stacking results of the northeast back azimuth events as a supplement (Fig. 4). The results of the two different back azimuths can reflect the crustal thicknesses of the both sides of the survey line respectively because of their different ray paths. Fig. 4b further shows that there is a dislocation of the Moho about 1– 2 km on the opposite sides of the WYFZ, and the inclinations of the Moho seem to be opposite.

In addition, crustal thicknesses can also be extracted from CCP images (Fig. 3b). However, due to the differences in models and methods, there is a little deviation (~1 km) between CCP imaging and H-κ stacking for crustal thicknesses (Fig. 5a), which means that the lateral variations of the Moho around the WYFZ are so small that it still may be within the error range. In order to demonstrate this feature, Moho depths are extracted from three longitudinal CCP stacking profiles (Figs. 5b-5d), in which BB' profile is along the WYFZ, and the other two profiles are on the opposite sides. Data of the temporary dense array and several regional permanent stations were used together for CCP imaging. Only the events of the northeast back azimuth (30° ~ 60°) were included, because this back azimuth is nearly perpendicular to the survey line and therefore can better reflect the lateral variations of the Moho. Similarly, the results also show that the inclinations of the Moho on the opposite sides of the WYFZ are different, with an average dislocation of the Moho about 1– 2 km. The common image features indicate that the lateral variations of the Moho around the WYFZ are robust, irrespective of the imaging method used.

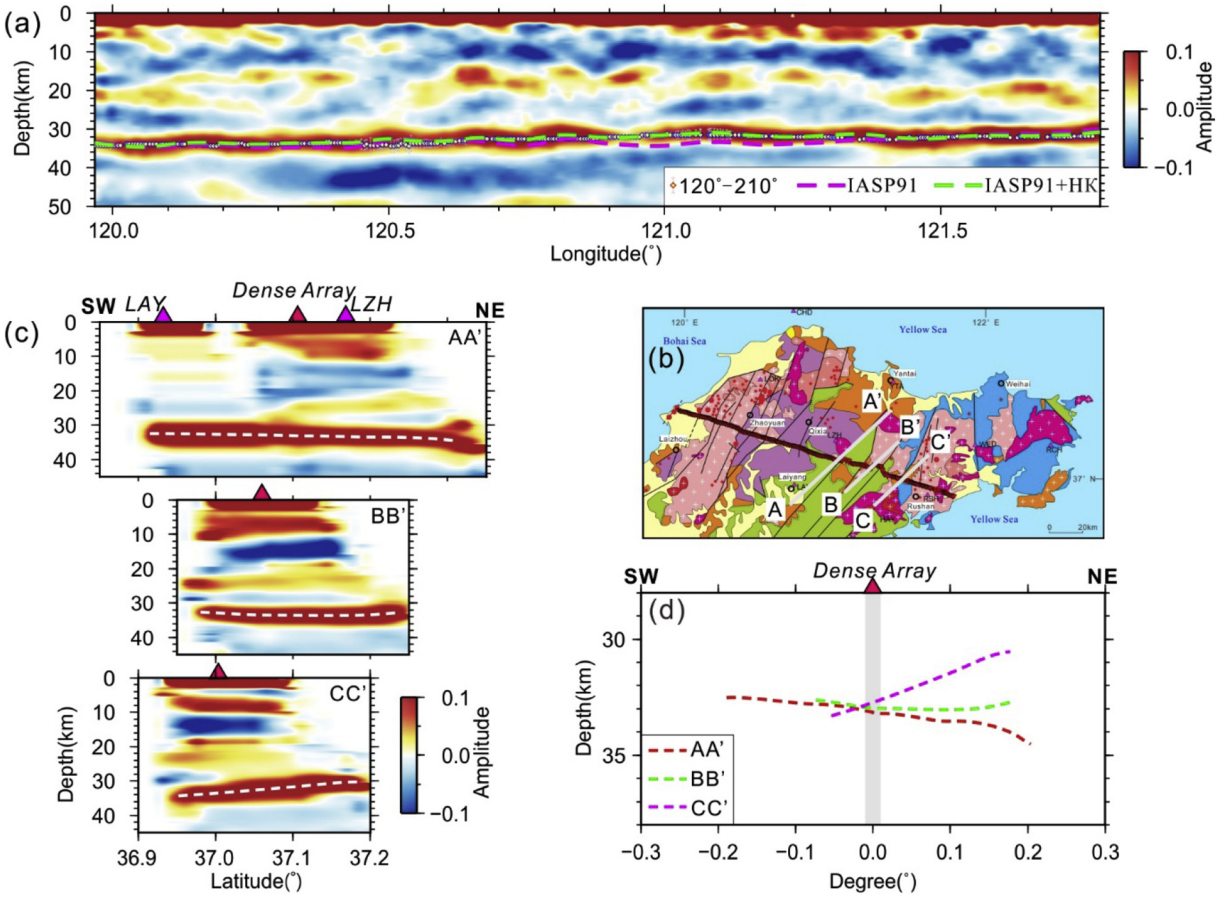

Fig. 5. Depth variations of Moho on the opposite sides of the Wulian-Yantai Fault Zone. (a) CCP image of the southeast back azimuth events (120°-210°) based on a fine velocity model (crustal thickness = 33 km, crustal Vp = 6.3 km/s, Vp/Vs ratios referred by H-κ stacking, mantle velocity referred by IASP91 model). Moho depths extracted from the CCP images based on fine velocity model and IASP91 model are marked by green and pink dotted line, respectively, which are shown together with the crustal thicknesses from H-κ stacking (yellow diamond). (b) The location of three CCP stacking profiles along the main tectonic strike (from north to east 43°). Only the northeast back azimuth events (30°-60°) are used, including both short-period dense array and regional broadband permanent stations. BB' profile coincides with the Wulian-Yantai Fault Zone. AA' and CC' profile are located on the opposite sides of the fault zone (about 20 km away). Three corresponding CCP images based on IASP91 model are shown as (c). Moho depth curves extracted from (c) are shown as (d) (aligned with the position of dense array). (For interpretation of the references to colour in this figure legend, the reader is referred to the web version of this article.)

4.2. Intracrustal velocity discontinuities

Furthermore, it's worth noting that there is a laterally trackable negative phase at ~12 km in the CCP image (Fig. 3b). We speculate that this negative phase may be a low-velocity discontinuity (LVD). However, intracrustal phases of P-wave receiver functions usually are difficult to identify, because of the mixing of primary and multiple phases, especially before 2 s. In order to identify the phases converted from main velocity discontinuities, one-dimensional synthetics of receiver function (Fig. 6) were carried out by referring to the main features of our data and regional velocity models (Ma et al., 1991; Zheng et al., 2008b; Jia et al., 2014; Pan et al., 2015; Meng et al., 2019). The results show that PsPs + PpSs multiple from the crystalline basement (2 km) and Ps conversion from the LVD (12 km) are all concentrated at about 1.5 s (Fig. 6a, M1 and M2), making it difficult to identify the intracrustal negative phase. Fortunately, multiple phases from the LVD appear after Ps conversion from the Moho in the synthetics (Fig. 6, M2 and M4), and the well-developed multiple phases can also be identified clearly in the actual data (Figs. 7a-b, Fig. S5). Thus, the strong negative phase coherently observed around 12 km (Fig. 3b) likely represents a true LVD in the crust, and it seems possible to further constrain its depth by using its multiple phases.

Also note that there is a group of high velocity discontinuities (HVD) at about 16– 20 km depth in the CCP image (Fig. 3b). The LVD and the HVD may constitute the top and the bottom interfaces of an intracrustal LVZ, respectively. Unfortunately, multiple phases of the HVD are weak and diffused, and are unable to be used to further constraint the properties of the HVD, obviously different from the LVD. Combining the above imaging results, we conclude that the LVD is a sharp velocity discontinuity and is slightly shallow beneath the Jiaolai basin, while the HVD is composed of a group of discontinuities. Specifically, the HVD is inclined to north beneath Jiaolai basin, and is relatively weak in the northwest Jiaodong Peninsula, indicating that the vertical velocity gradient may be small. Moreover, on the opposite sides of the WYFZ, all of the three major velocity discontinuities including the LVD, the HVD and the Moho, have a dislocation to different degrees. Detachment faults represented by the Zhaoping fault with a SE inclination can also be identified from the high-quality imaging results (Fig. 3b), benefited from dense data coverage.

For the reason mentioned in section 3, we mainly use the teleseismic events of the southeast back azimuth. To analyze whether the above features are robust, we compare the CCP images using data of different back azimuths (Fig. S2). The results show that no matter which back azimuth is adopted, the negative seismic phase at about 12 km and the positive seismic phase at about 16– 20 km always exist, indicating that the main crustal features are robust. Although there are some differences in the amplitude and depth, the differences are small as a whole. Generally, dipping structures or seismic anisotropy will cause periodic

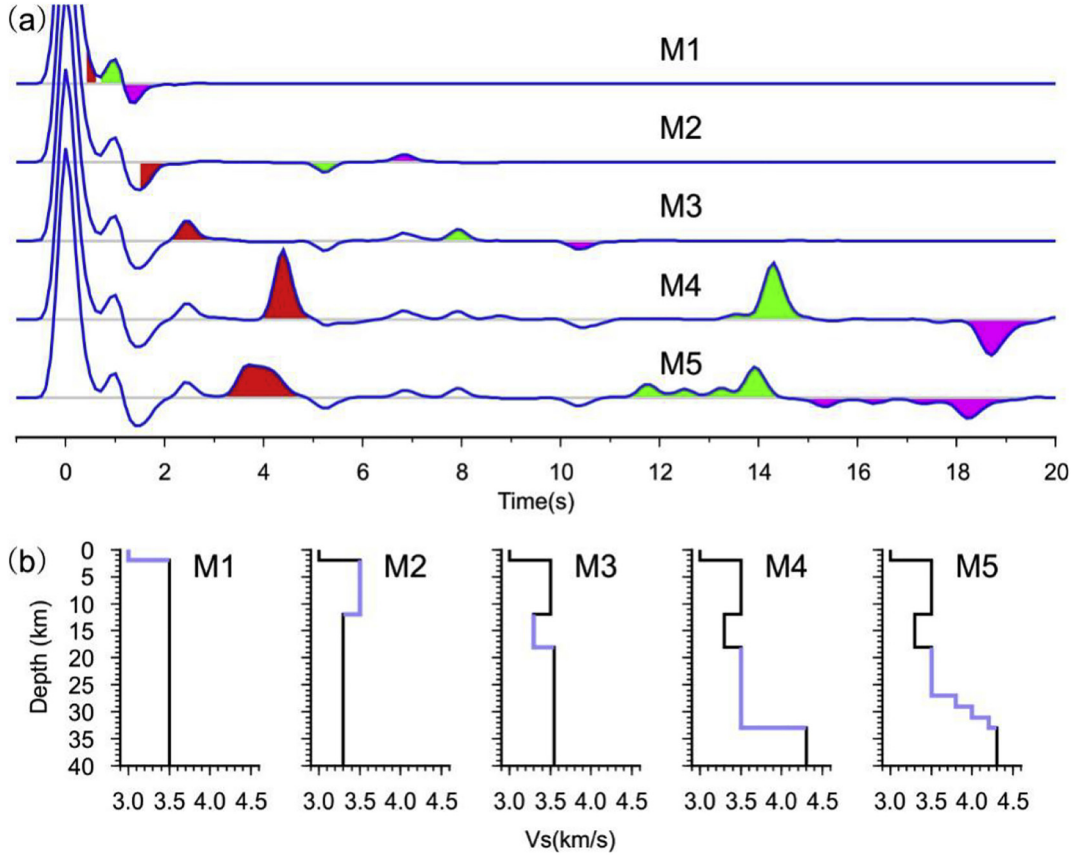

Fig. 6. Multiple phase analysis for the main crustal velocity discontinuities. (a) One-dimensional synthetics of the receiver function based on five models (M1, M2, M3, M4 and M5), respectively. (b) S-wave velocity of the five models, which add a crystalline basement (2 km depth), an intracrustal LVD (12 km depth), an intracrustal HVD (18 km depth), a sharp Moho (33 km depth) and a thick crust-mantle transition zone (27– 33 km), respectively. The corresponding velocity discontinuities are marked with blue, and their Ps, PpPs and PpSs + PsPs phases are marked with red, green and pink in (a) respectively. (For interpretation of the references to colour in this figure legend, the reader is referred to the web version of this article.)

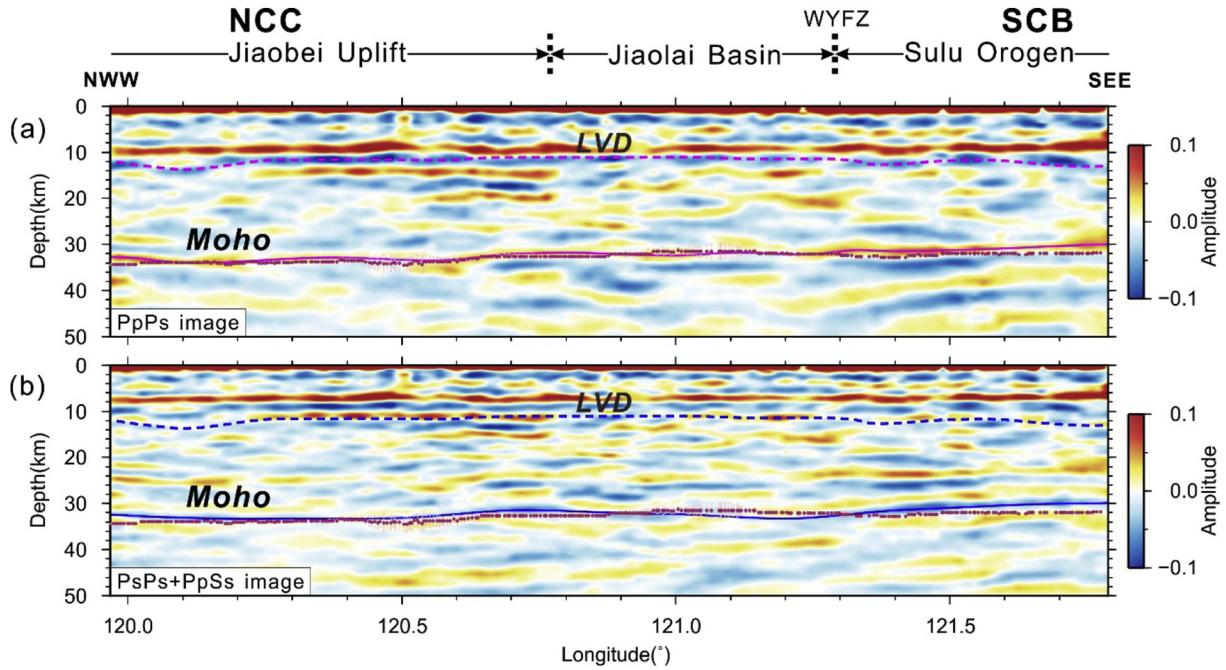

Fig. 7. CCP images of multiple phases. (a) and (b) are images of PpPs and PsPs + PpSs phases (0.01– 1.2 Hz), respectively. Dotted line and solid line denote LVD and Moho, respectively. Red diamond denotes the crustal thickness from H-κ stacking. (For interpretation of the references to colour in this figure legend, the reader is referred to the web version of this article.)

changes of receiver functions' phases with the change of back azimuths. Considering the changes of the main phases are small with the change of back azimuths, we think the influences of dipping structures and seismic anisotropy can be ignored here. In addition, the deep seismic sounding profile (Pan et al., 2015) across the Jiaodong Peninsula has observed two group of reflection phases from two intracrustal interfaces. The depths of the two interfaces are consistent well with the LVD and the HVD presented in this paper, which also indicates the robustness of our results.

4.3. Vp/Vs ratio

Based on the well-developed multiple phases of the LVD, we further carried out the H-κ stacking of the upper crust (above the LVD) for the three major tectonic units (Jiaobei uplift, Jiaolai basin and Sulu orogenic belt). To improve the signal-to-noise ratios, stations are divided into three groups (stations 001–130, 131–250 and 251–340 are included, respectively), and receiver functions of each group are used together to obtain only one H-κ stacking result (Fig. 3e, Fig. S5). According to the whole crustal (Fig. 3d) and upper crustal H-κ stacking results, the lower crustal Vp/Vs ratios (Fig. 3e) were calculated by using a linear weighted calculation formula (Wang et al., 2018).

$$H_{upper} \times \kappa_{upper} + H_{lower} \times \kappa_{lower} = H_{crust} \times \kappa_{crust} \quad (1)$$

The whole crustal H-κ stacking results (Fig. 3d) show that average crustal Vp/Vs ratio of the Jiaodong Peninsula is about 1.76, comparable to the global average (Christensen, 1996). The Vp/Vs ratio in the Jiaolai Basin is the highest (1.79) among the three tectonic units. Furthermore, layered H-κ stacking results (Fig. 3e) show that average Vp/Vs ratios of the lower crust in the three tectonic units are not significantly different, but average Vp/Vs ratios of the upper crust in the Jiaobei uplift and the Sulu orogenic belt are obviously low, corresponding to the relatively low (≤average value) Bouguer gravity anomalies (Fig. 3c) and the outcrops of granite on the surface (Fig. 3a).

4.4. Properties of crust-mantle transition zone

Multiple phases can well reflect the properties of crust-mantle transition zone (CMTZ) (Fig. 6, M4 and M5), and the thickness of the CMTZ can be estimated by S-wave velocity inversion of receiver functions (Zheng et al., 2008a). Stacked receiver functions of the profile (Fig. S4a) show that, PpPms phases (12– 14 s) from the Moho are weak and diffused in the Jiaobei uplift and the Jiaolai basin, but are strong and clear to be traced in the Sulu orogenic belt. With regards to this, we selected 5 short-period seismic stations (equally spaced) and 6 broadband permanent stations to carry out the S-wave velocity inversion of receiver functions (Fig. 8, Fig. S6, Fig. S7). In order to improve the signal-to-noise ratios of the short-period data, we sacrificed the lateral resolution properly by using the inversion result of a stacked receiver function of 11 adjacent stations as the result of central station. Considering that receiver function inversion is insensitive to absolute velocity and has multiple solutions, we took the average Vs model of the eastern NCC (Ma et al., 1991; Zheng et al., 2008b; Jia et al., 2014; Pan et al., 2015; Meng et al., 2019) and our H-κ stacking results as important prior constraints in the inversion process. Based on the understanding of the major velocity discontinuities and their multiple phases (Fig. 6), we further carried out the waveform inversion (Fig. S7) of receiver functions by using CPS330 (Herrmann, 2013).

The detailed analyses of the results are shown as Fig. 8. By comparing the synthetic receiver functions (Fig. 8a, blue solid line) calculated from the inverted velocity models with the actual data (Fig. 8a, gray dotted line), we identified that the Ps phases near 3.5– 4.5 s and the following PpPs phases near 11– 15 s are generated by the CMTZ. In this paper, the CMTZ is defined from the layer with obvious increasing of Vs below 25 km to the Moho surface. Statistics of the inversion results (Fig. 8b and c) show that the CMTZ is thin in the Sulu orogenic belt, but is thick in the Jiaobei uplift and the Jiaolai basin. This feature is consistent with the results of deep seismic sounding (Pan et al., 2015).

5. Discussion

5.1. Widespread crustal extension beneath the Jiaodong Peninsula

In the Mesozoic-Cenozoic, like other areas in the eastern China, the Jiaodong Peninsula has undergone intense continental extension. Large-scale extensional structures represented by the Linglong MCC and the Jiaolai faulted basin have been formed on the surface (Lin and Wei, 2018). However, high-resolution seismic observations of the crustal extension have been scarce. Based on the teleseismic data recorded by a short-period dense seismic array, we are able to image the crustal structure beneath the Jiaodong Peninsula in detail.

The fine crustal images show that a LVZ is generally developed at about 12– 16 km depth. The LVZ has been reported in previous seismological researches of the Jiaodong Peninsula and its adjacent areas (Zheng et al., 2008b; Jia et al., 2014; Pan et al., 2015; Meng et al., 2019), corresponding to a high-conductivity layer in magnetotelluric results (Zhang et al., 2018), yet its authenticity and tectonic significance are still controversial. In our CCP images, the top interface (LVD) of the LVZ is coherently identified through the analysis of multiple phases, demonstrating the existence of the LVZ. Moreover, statistics (Fig. 3e, gray circles) show that historical earthquakes within 10 km on both sides of the survey line are mainly concentrated above 12 km, consistent with the depth of the LVD. Therefore, the physical meaning of the top interface of the LVZ becomes clear, because it is generally believed that the maximum focal depth corresponds to the brittle-ductile transition zone (Liu et al., 2016; Petricca et al., 2018). In addition, we speculate that the feature of low-velocity may be caused by water or saline fluids. This kind of interpretation is strongly supported by the study of Kola superdeep well (Kozlovsky, 1987), and is similar to the interpretations for many other intracrustal low-velocity layers found in the world (Marquis and Hyndman, 1992; Xu et al., 2019). As for the source of water, we infer it may be attributed to the dehydration of the subducted and stagnant Paleo-Pacific slab in the mantle transition zone, which may lead to the weakening of overlying lithosphere, partial melting of the crust and mantle, and voluminous magmatism (Campbell and Taylor, 1983; Thompson, 1999; Niu, 2005, 2014; Menzies et al., 2007; Zhu and Zheng, 2009; Zhu et al., 2015). The water may remain to the present day under the weak extensional setting in the Cenozoic. Certainly, partial melting may also be a kind of interpretation for the LVZ, but we don't support it because the resistivity of the LVZ and the surficial heat flow values in the Jiaodong Peninsula are only comparable to the global continental average (Martyn, 2003) and the Chinese continental average (Jiang et al., 2019), respectively. Thus, we speculate that the LVZ at about 12– 16 km is a brittle-ductile transition zone with water or saline fluids and has been formed under the strong extensional setting in the Mesozoic-Cenozoic.

More interestingly, the bottom (HVD) of the LVZ beneath the Jiaolai basin is composed of a group of north-dipping interfaces. Considering the two important geological events since the Mesozoic, we infer that the north-dipping interfaces may be a series of thrust nappe structures formed during the Triassic continental collision, or exhumation channels of UHPM rocks formed after the collision, or detachment faults formed under the extensional setting since the Late Mesozoic. However, the relatively flat Moho indicates that Triassic thrust nappe structures have been difficult to be preserved so well under the strong crustal modification since the Late Mesozoic. Furthermore, as we know that detachment faults are generally developed in the brittle-ductile transition zone of middle crust at about 15 km depth (Davis, 1983), but the north-dipping interfaces here appear in the lower crust. Therefore, the interpretation like detachment faults is also not convincing. Further considering the distribution of UHPM rocks and their multistage

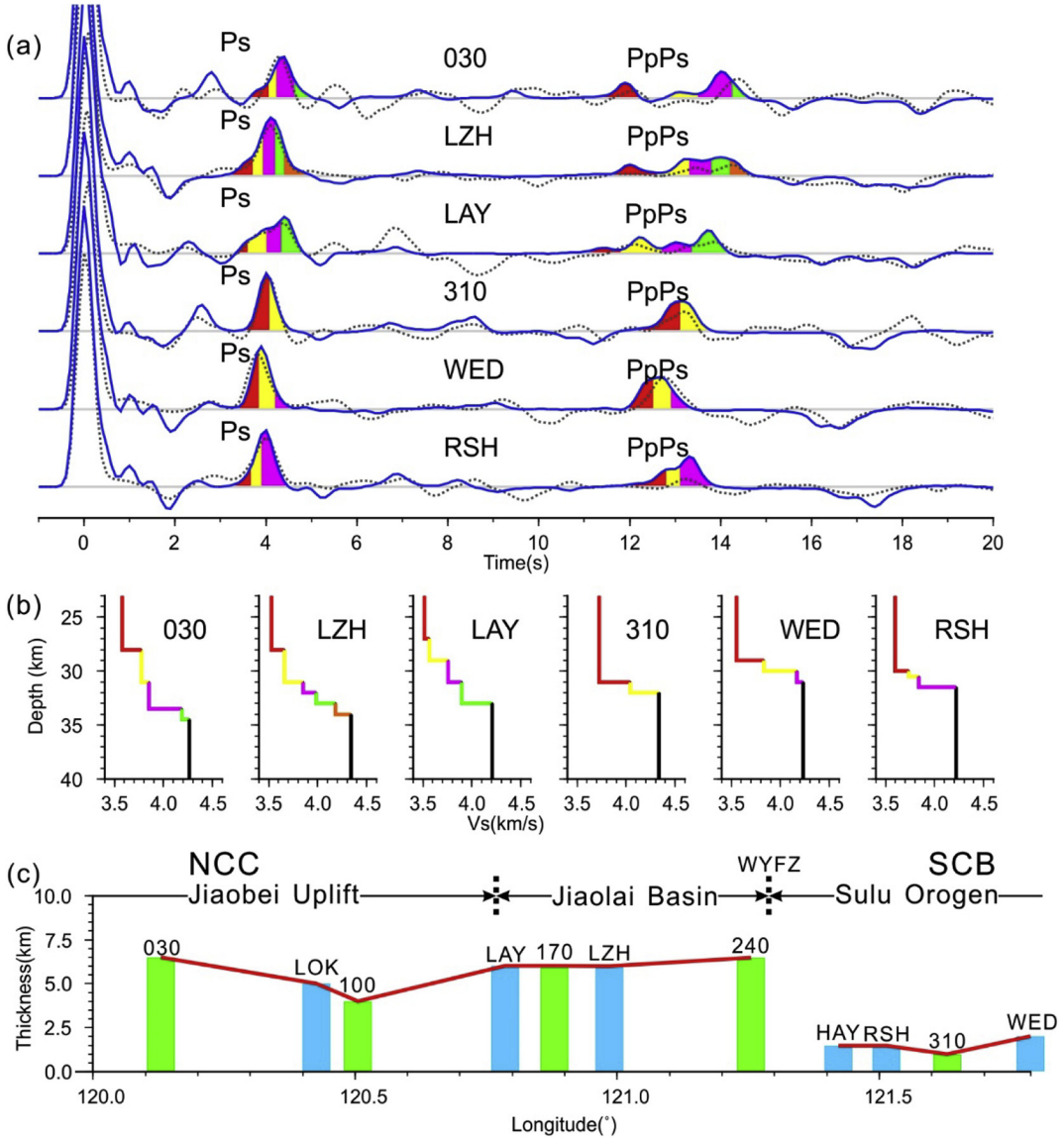

Fig. 8. S-wave velocity inversion of receiver functions. (a) Waveform comparison between the observed receiver function (gray dotted line) and the synthetics (blue solid line). (b) The inverted optimal velocity models (see Fig. S7 for details). The arrivals of Ps and PpPs phases converted from multiple discontinuities of the crust-mantle transition zone (CMTZ) are marked with different colors in (a), corresponding to (b). (c) Statistics for the thicknesses of CMTZ. Results of different stations are projected to the profile along the perpendicular direction of the survey line. 030, 100, 170, 240 and 310 are short-period stations. LOK, LAY, LZH, HAY, RSH, and WED are broadband permanent stations. (For interpretation of the references to colour in this figure legend, the reader is referred to the web version of this article.)

exhumations from early to late stage of the collision (Lin et al., 2013), we finally speculate that the north-dipping interfaces may be a series of thrust nappe structures formed in the early stage of the collision, and reactivated to be the exhumation channels of UHPM rocks at later under the extensional setting. In other words, the north-dipping interfaces beneath the Jiaolai basin may also be extensional structures in a broad sense.

5.2. Intense extension and magmatism beneath the northwest Jiaodong metallogenic belt

Except for the above-mentioned extensional structures of the whole region, our detailed imaging results also imply that crustal extension and magmatism have been especially intense in the northwest Jiaodong metallogenic belt since the Late Mesozoic, with evidences existing at different crustal scales from the upper crust to the CMTZ. First of all, large-scale ore-controlling detachment faults, represented by the Zhaoping fault zone, can be identified in the brittle upper crust. CCP images show that these detachment faults are mainly southeast-oriented and converge to the brittle-ductile transition zone at about 12 km. To the upper part of the lower crust, characteristics of the HVD are very weak, indicating a small vertical velocity gradient. Accordingly, we infer that the northwest Jiaodong may have undergone strong vertical magmatic or hydrothermal activities since the Late Mesozoic, which may destroyed the original horizontal layered structures. Moreover, the thick CMTZ of the Jiaobei terrane (including the Jiaobei uplift and the Jiaolai basin) indicates a secular interaction between the crust and the underlying mantle, and implies magmatic underplating may have occurred. This interpretation is supported by the study of Guojialing granodiorites (Yang et al., 2003b). The above seismic evidences indicate that both of the brittle-ductile transition zone and the lower crust beneath the northwest Jiaodong once may be extremely weak, and endmember numerical simulations carried out by Lu et al. (2016) have shown that these kind of conditions are conductive to the formation of MCC, which means that the theory of MCC corresponds well with the actual observations of the Linglong MCC (or

extensional dome) in the northwest Jiaodong. Therefore, we propose that the intense crustal extension beneath the northwest Jiaodong metallogenic belt may be manifested not only by the detachment faults in the brittle upper crust, but also by the vertical magmatic or hydrothermal activities caused by transverse extension in the ductile lower crust and the CMTZ, and these seismic evidences at different crustal scales are organically linked.

5.3. Strike-slip properties of the WYFZ beneath the Muru metallogenic belt

As an important ore-controlling structure in the Muru metallogenic belt, the WYFZ is a brittle strike-slip fault zone observed from the surface (Zhai et al., 2000; Zhang et al., 2007), different from other ore-controlling structures dominated by extensional detachments faults in the region. However, the scale of the WYFZ and its tectonic significance are still controversial (Faure et al., 2001; Zheng et al., 2005; Zhou et al., 2008), due to the stacking influences of multistage tectonic activities since the Mesozoic, mainly including the continental collision in the Triassic, the left strike-slip in the Late Jurassic, the extension with the formation of Jiaolai basin in the Early Cretaceous, and the weak right strike-slip in the Paleogene. Fortunately, our fine-scale imaging results show that there are significant crustal structure differences on the opposite sides of the WYFZ, in the depth and structure of the Moho, intracrustal LVZ, upper crustal Vp/Vs ratios, and Bouguer gravity anomalies, indicating that the WYFZ may be a steep transcrustal fault. It is interesting to analyze the influences of different geological processes in different periods.

The UHPM rocks distributed in the southeast of the WYFZ has clearly revealed the deep continental subduction event in the Triassic, and therefore the WYFZ is generally considered as the Triassic suture. However, the overall flat Moho in the CCP images indicates that the lower crust beneath the Jiaodong Peninsula may have been extensively modified. So this steep fault may mainly form after the Triassic continental collision. As for its linkage with the Triassic suture still need further demonstration. On the other hand, the WYFZ is also considered as the tectonic boundary of the Jiaolai faulted basin in the Early Cretaceous (Li et al., 2007; Zhou et al., 2008), but it is difficult for a normal fault to cut through the crust and to result in the opposite inclinations of the Moho on both sides of the fault zone. After further excluding the weak influence in the Paleogene, we speculate that the steep geometry and deep penetration features of the WYFZ may be caused by the strike-slip since the Late Jurassic.

In addition, we infer that the relatively low upper crustal Vp/Vs ratios and Bouguer gravity anomalies in the southeast of the WYFZ may be mainly influenced by the distribution of large-scale Mesozoic granites (biased to felsic and low density) (Sobolev and Babeyko, 1994; Zhang and Zhang, 2007), because same characteristics can be found in the Jiaobei uplift. As for the high upper crustal Vp/Vs ratio of the Jiaolai basin, we think it is a relative feature between the Precambrian rocks (mainly developed in the edge of the Jiaolai Basin) and the Mesozoic granites (mainly developed in the Jiaobei uplift and the Sulu orogenic belt). We don't interpret too much here. In summary, both the physical and geometric properties on the opposite sides of the WYFZ cannot be regarded as independent evidences for the Triassic suture, but they indicate that the WYFZ may be a steep transcrustal fault and act as a tectonic boundary between the Sulu orogenic belt and the Jiaobei terrane.

5.4. The linkage between the tectonic-magmatic activities and the gold mineralization

The detailed crustal structure image not only shows the characteristics of widespread crustal extension beneath the Jiaodong Peninsula, but also clearly delineates the structural differences between the northwest Jiaodong metallogenic belt and the Muru metallogenic belt. Thus, further comparative study of the two metallogenic belts is required to analyze the causes of regional metallogenic differences, and to further reveal the linkage between the gold mineralization and the intense tectonic-magmatic activities.

Although geologists have done a lot of researches from the perspective of ore-host rocks and ore-forming fluids (Yang et al., 2014; Li et al., 2015; Song, 2015), the uneven gold distribution has always been a matter of great concern. Based on the fine images of the crustal structure, we will try to discuss the uneven gold distribution from the perspective of extension structure, magmatism and their intrinsic connection. As we know, large-scale and similar types of Mesozoic granites are generally developed in both of the two metallogenic belts (Fig. 1b) (Zhang and Zhang, 2007). Therefore, although magma is an important source of ore-forming fluids, neither its scale nor type is likely to be the controlling factor of regional metallogenic differences. Actually, large and super-large gold deposits are mainly controlled by large-scale detachment faults (Fig. 1b). Therefore, it is necessary to consider the intrinsic relationship between extensional structures and magmatism. Although extensional structures are widely developed in the whole Jiaodong Peninsula, the structural differences between the east and the west are also obvious. In the northwest Jiaodong, CCP images show that detachment faults are widely developed in the upper crust, and strong vertical magmatic or hydrothermal activities may have occurred in the lower crust and the CMTZ. Accordingly, we infer that the coupled effects of intense crustal extension, voluminous magmatism and water released from the subducting Paleo-Pacific slab may have been responsible for the highly concentrated gold deposits in the northwest Jiaodong metallogenic belt. While the Muru metallogenic belt is mainly controlled by the WYFZ with strike-slip characteristics (Yang et al., 2014; Song et al., 2015). The deep fault zone may have acted as a channel for magma upwelling, but it may not be conducive to the precipitation of gold due to its large dip.

Jiaodong gold mineralization and the destruction of the NCC are highly coupled in time-space relationships, indicating that their dynamic mechanisms may also be related (Zhu et al., 2015). We support that the westward subduction of the Paleo-Pacific Plate, which destabilized the mantle convection system, mainly contributed to the lithospheric thinning and provided an important source of mantle-derived fluids for the gold mineralization in the eastern China (Niu, 2005, 2014; Menzies et al., 2007; Zhu and Zheng, 2009; Zhu et al., 2015). However, the specific mechanisms in different regions may be different. The contrasted thicknesses of the CMTZ on the opposite sides of the WYFZ indicate that the forms of crust-mantle interaction may be different. The thick CMTZ in the Jiaobei terrane indicates that magmatic underplating may have occurred since the Late Mesozoic (Yang et al., 2003b). On the contrary, the sharp CMTZ in the Sulu orogenic belt indicates that the huge thick mountain roots mainly composed of high density eclogite may have disappeared gradually by delamination because of the gravitational instability in the late stage (Gao et al., 1999). This interpretation is supported by the geochemical studies of granulites in the Sulu area (Ying et al., 2013). Certainly, other geodynamic actions like the lithospheric extension may also play important roles, although the magmatic underplating and the delamination can well explain the above differences of the CMTZ, respectively. Thus, more evidences from petrology, geochemistry, geophysics and other disciplines are necessary for understanding the dynamic mechanisms of the NCC destruction and the Jiaodong gold mineralization and their genetic linkage more comprehensively.

6. Conclusions

From the research of receiver functions based on a linear short-period dense seismic array, the crustal structure beneath the Jiaodong Peninsula is well imaged, and we propose the following preliminary conclusions:

(1) The average crustal thickness is 33 km, and the average crustal Vp/

Vs is ~1.76. The LVZ developed at 12– 16 km depth may be a brittle-ductile transition zone with water or saline fluids. The north-dipping interfaces beneath the Jiaolai basin may be a series of thrust nappe structures formed during the Triassic collision, and reactivated as the exhumation channels of UHPM rocks in the later. The formation of the LVZ or activation of the north-dipping interfaces may be attributed to the extensional setting since the Late Mesozoic, and they both imply the widespread crustal extension beneath the Jiaodong Peninsula.

(2) Crustal extension are especially intense in the northwest Jiaodong metallogenic belt, reflected in different crustal scales. On the one hand, detachment faults indicate the transverse extension in the brittle upper crust. On the other hand, the small vertical velocity gradient of the HVD, as well as the thick CMTZ imply the vertical magmatic or hydrothermal activities in the ductile lower crust, which may be also caused by transverse extension.

(3) The Muru metallogenic belt are mainly controlled by the WYFZ, which is a strike-slip fault zone. Significant differences of the Moho, intracrustal LVZ, upper crustal Vp/Vs ratios, and Bouguer gravity anomalies are found on the opposite sides of the WYFZ, indicating that the WYFZ may be a steep transcrustal fault and act as a tectonic boundary between the Sulu orogenic belt and the Jiaobei terrane.

(4) The structural differences may contribute to the metallogenic differences between the east and the west of the Jiaodong Peninsula. The coupling of intense crustal extension, voluminous magmatism and water released from the subducting Paleo-Pacific slab may be significant causes of the concentrated gold deposits in the northwest Jiaodong metallogenic belt during the peak of the NCC destruction. While the Muru metallogenic belt is mainly controlled by the WYFZ, which may not be conducive to the precipitation of gold due to its large dip and weak extension.

Declaration of Competing Interest

The authors declare that they have no known competing financial interests or personal relationships that could have appeared to influence the work reported in this paper.

Acknowledgments

We thank Profs. Tianyu Zheng, Wei Lin and Dr. Lingtong Meng for their helpful discussions. Thanks for the field data acquisition work of the Short-Period Seismograph Observation Laboratory, IGGCAS. Seismic data of permanent stations are provided by the Data Management Center of China National Seismic Network at Insitute of Geophysics (SEISDMC, doi:10.11998/SeisDmc/SN, http://www.seisdmc.ac.cn; Zheng et al., 2010). This work was supported by the National Key Research and Development Program of China (Grant No. 2016YFC0600101).

Appendix A. Supplementary data

Supplementary data to this article can be found online at https://doi.org/10.1016/j.tecto.2020.228532.

References

Campbell, I.H., Taylor, S.R., 1983. No water, no granites-no oceans, no continents. Geophy. Res. Lett. 10, 1061–1064. https://doi.org/10.1029/gl010i011p01061.

Carlson, R.W., Pearson, D.G., James, D.E., 2005. Physical, chemical, and chronological characteristics of continental mantle. Rev. Geophys. 43, RG1001. https://doi.org/10.1029/2004RG000156.

Chen, L., 2010. Concordant structural variations from the surface to the base of the upper mantle in the North China Craton and its tectonic implications. Lithos 120, 96–115. https://doi.org/10.1016/j.lithos.2009.12.007.

Chen, L., Zheng, T.Y., Xu, W.W., 2006. A thinned lithospheric image of the Tanlu Fault Zone, Eastern China: Constructed from wave equation based receiver function migration. J. Geophys. Res. 111, B09312. https://doi.org/10.1029/2005JB003974.

Chen, L., Wang, T., Zhao, L., Zheng, T.Y., 2008. Distinct lateral variation of lithospheric thickness in the Northeastern North China Craton. Earth Planet. Sci. Lett. 267, 56–68. https://doi.org/10.1016/j.epsl.2007.11.024.

Chen, L., Cheng, C., Wei, Z.G., 2009. Seismic evidence for significant lateral variations in lithospheric thickness beneath the central and western North China Craton. Earth Planet. Sci. Lett. 286, 171–183. https://doi.org/10.1016/j.epsl.2009.06.022.

Christensen, N.I., 1996. Poisson's ratio and crustal seismology. J. Geophys. Res. Solid Earth 101, 3139–3156. https://doi.org/10.1029/95JB03446.

Davis, G.H., 1983. Shear-zone model for the origin of metamorphic core complexes. Geology 11, 342–347.

Deng, J., Liu, X.F., Wang, Q.F., Pan, R.G., 2014. Origin of the Jiaodong-type Xinli gold deposit, Jiaodong Peninsula, China: Constraints from fluid inclusion and C-D-O-S-Sr isotope compositions. Ore Geol. Rev. 65, 674–686. https://doi.org/10.1016/j.oregeorev.2014.04.018.

Fan, H.R., Zhai, M.G., Xie, Y.H., Yang, J.H., 2003. Ore-forming fluids associated with granite-hosted gold mineralization at the Sanshandao deposit, Jiaodong gold province, China. Miner. Depos. 38, 739–750. https://doi.org/10.1007/s00126-003-0368-x.

Faure, M., Lin, W., Breton, N.L., 2001. Where is the North China-South China block boundary in eastern China? Geology 29 (2), 119–122.

Gao, S., Zhang, B.R., Jin, Z.M., 1999. Lower crustal delamination in the Qinling-Dabie orogenic belt. Sci. China Ser. D 42 (4), 423–433.

Gilder, S.A., Leloup, P.H., Courtillot, V., Chen, Y., Coe, S.R., Zhao, X., Xiao, W., Halim, N., Cogné, J.P., Zhu, R., 1999. Tectonic evolution of the Tancheng-Lujiang (Tan-Lu) fault via Middle Triassic to early Cenozoic paleomagnetic data. J. Geophys. Res. 104, 15365–15390. https://doi.org/10.1029/1999JB900123.

Goldfarb, R.J., Santosh, M., 2014. The dilemma of the Jiaodong gold deposits: are they unique? Geosci. Front. 5, 139–153. https://doi.org/10.1016/j.gsf.2013.11.001.

Goldfarb, R., Groves, D.I., Gardoll, S., 2001. Orogenic gold and geologic time: a global synthesis. Ore Geol. Rev. 18, 1–75. https://doi.org/10.1016/S0169-1368(01)00016-6.

Groves, D.I., Goldfarb, R.J., Gebre-Mariam, M., Hagemann, S.G., Robert, F., 1998. Orogenic gold deposits: a proposed classification in the context of their crustal distribution and relationship to other gold deposit types. Ore Geol. Rev. 13, 7–27. https://doi.org/10.1016/S0169-1368(97)00012-7.

Herrmann, R.B., 2013. Computer programs in seismology: an evolving tool for instruction and research. Seismol. Res. Lett. 84, 1081–1088. https://doi.org/10.1785/0220110096.

Jia, S.X., Wang, F.Y., Tian, X.F., Duan, Y.H., Zhang, J.S., Liu, B.F., Lin, J.Y., 2014. Crustal structure and tectonic study of North China Craton from a long seismic sounding profile. Tectonophysics 627, 48–56. https://doi.org/10.1016/j.tecto.2014.04.013.

Jiang, G.Z., Hu, S.B., Shi, Y.Z., Zhang, C., Wang, Z.T., Hu, D., 2019. Terrestrial heat flow of continental China: Updated dataset and tectonic implications. Tectonophysics 753, 36–48. https://doi.org/10.1016/j.tecto.2019.01.006.

Kennett, B.L.N., Engdahl, E.R., 1991. Travel times for global earthquake location and phase identification. Geophys. J. Int. 105, 429–465. https://doi.org/10.1111/j.1365-246X.1991.tb06724.x.

Kozlovsky, Y.A., 1987. The Superdeep Well of the Kola Peninsula. Springer Verlag, Berlin.

Langston, C.A., 1979. Structure under Mount Rainier, Washington, inferred from teleseismic body waves. J. Geophys. Res. 84, 4749–4762. https://doi.org/10.1029/JB084iB09p04749.

Li, Z.X., 1994. Collision between the North and South China blocks: a crustal-detachment model for suturing in the region east of the Tanlu fault. Geology 22 (8), 739–742.

Li, S.G., Xiao, Y.L., Liou, D.L., Chen, Y.Z., Ge, N.J., Zhang, Z.Q., Sun, S.S., Cong, B.L., Zhang, R.Y., Hart, S.R., Wang, S.S., 1993. Collision of the North China and Yangtse Blocks and formation of coesite-bearing eclogites: timing and processes. Chem. Geol. 109, 89–111. https://doi.org/10.1016/0009-2541(93)90063-O.

Li, J.L., Zhang, Y.Q., Liu, Z.Q., Ren, F.L., Yuan, J.Y., 2007. Sedimentary-subsidence history and tectonic evolution of the Jiaolai basin, eastern China. Geol. China 34 (2), 240–250 (in Chinese with English abstract).

Li, H.k., Zhuo, C.Y., Gen, K., Liang, T.T., 2012. Study on tectonic background of gold mineralization in Jiaodong area. Shandong Land and Resources 28 (1), 5–13 (in Chinese with English abstract).

Li, L., Santosh, M., Li, S.R., 2015. The 'Jiaodong type' gold deposits: Characteristics, origin and prospecting. Ore Geol. Rev. 65, 589–611. https://doi.org/10.1016/j.oregeorev.2014.06.021.

Li, C.L., Chen, C.X., Dong, D.D., Kuponiyi, A.P., Dosso, S.E., Su, D.L., 2018. Ambient noise tomography of the Shandong province and its implication for Cenozoic intraplate volcanism in eastern China. Geochem. Geophys. Geosyst. 19, 3286–3301. https://doi.org/10.1029/2018GC007515.

Ligorría, J.P., Ammon, C.J., 1999. Iterative deconvolution and receiver function estimation. Bull. Seism. Soc. Am. 89 (5), 1395–1400.

Lin, W., Wei, W., 2018. Late Mesozoic extensional tectonics in the North China Craton and its adjacent regions: a review and synthesis. Int. Geol. Rev. https://doi.org/10.1080/00206814.2018.1477073.

Lin, W., Ji, W.B., Shi, Y.H., Chu, Y., Li, Q.L., Chen, Z.C., Liu, F., Wang, Q.C., 2013. Multi-stage exhumation processes of the UHP metamorphic rocks: Implications from the extensional structure of Tongbai-Hong'an-Dabieshan orogenic belt. Chin. Sci. Bull. 58, 2259–2265. https://doi.org/10.1360/972013-560.

Liu, S., Hu, R.Z., Zhao, J.H., Feng, C.X., Zhong, H., Cao, J.J., Shi, D.N., 2005. Geochemical characteristics and petrogenetic investigation of the late Mesozoic lamprophyres of Jiaobei, Shandong province. Acta Petrol. Sin. 21 (3), 947–958 (in Chinese with English abstract).

Liu, C., Zhu, B.J., Shi, Y.L., 2016. Lithospheric rheology and Moho upheaval control the generation mechanism of the intraplate earthquakes in the North China Basin. J. Asian Earth Sci. 121, 153–164. https://doi.org/10.1016/j.jseaes.2016.03.008.

Liu, Z., Tian, X, B., Gao, R., Wang, G. C., Wu, Z. B., Zhou, B. B., Tan, P., Nie, S. T., Yu, G. P., Zhu, G. H., Xu, X., 2017. New images of the crustal structure beneath eastern Tibet from a high-density seismic array. Earth Planet. Sci. Lett., 480, 33–41. doi:https://doi.org/10.1016/j.epsl.2017.09.048.

Lu, G., Zhao, L., Zheng, T.Y., Wang, K., Yang, J.F., 2016. Determining the key conditions for the formation of metamorphic core complexes by geodynamic modeling and insights into the destruction of North China Craton. Sci. China Earth Sci. 59 (9), 1873–1884. https://doi.org/10.1007/s11430-015-5407-5.

Ma, X.Y., Liu, C.Q., Liu, G.D., 1991. Xiangshui (Jiangsu province) to Mandal (Nei MonGGOL) geoscience transect. Acta Geol. Sin. 3, 199–215 (in Chinese with English abstract).

Mao, J.W., Wang, Y.T., Li, H.M., Pirajno, F., Zhang, C.Q., Wang, R.T., 2008. The relationship of mantle-derived fluids to gold metallogenesis in the Jiaodong Peninsula: evidence from D-O-C-S isotope systematics. Ore Geol. Rev. 33, 361–381. https://doi.org/10.1016/j.oregeorev.2007.01.003.

Marquis, G., Hyndman, R.D., 1992. Geophysical support for aqueous fluids in the deep crust: seismic and electrical relationships. Geophys. J. Int. 110, 91–105. https://doi.org/10.1111/j.1365-246X.1992.tb00716.x.

Martyn, U., 2003. Studying continental dynamics with magnetotelluric exploration. Earth Sci. Front. 10 (1), 25–38.

Meng, Y.F., Yao, H.J., Wang, X.Z., Li, L.L., Feng, J.K., Hong, D.Q., Wang, X.L., 2019. Crustal velocity structure and deformation features in the central-southern segment of Tanlu fault zone and its adjacent area from ambient noise tomography. Chin. J. Geophys. 62 (7), 2490–2509. in Chinese with English abstract. https://doi.org/10.6038/cjg2019M0189.

Menzies, M.A., Xu, Y.G., Zhang, H.F., Fan, H.R., 2007. Integration of geology, geophysics and geochemistry: a key to understanding the North China Craton. Lithos 96, 1–21. https://doi.org/10.1016/j.lithos.2006.09.008.

Niu, Y.L., 2005. Generation and evolution of basaltic magmas: some basic concepts and a hypothesis for the origin of the Mesozoic-Cenozoic volcanism in eastern China. Geol. J. China Univ. 11, 9–46.

Niu, Y.L., 2014. Geological understanding of plate tectonics: basic concepts, illustrations, examples and new perspectives. Global Tectonics and Metallogeny 10, 23–46. https://doi.org/10.1127/gtm/2014/0009.

Okay, A.I., Sengor, A.M.C., 1992. Evidence for continental thrust-related exhumation of the ultra-high pressure rocks in China. Geology 20, 411–414.

Pan, S.Z., Wang, F.Y., Zheng, Y.P., Duan, Y.L., Liu, L., Deng, X.G., Song, X.H., Sun, Y.N., Ma, C.J., Li, Y.Q., 2015. Crustal velocity structure beneath Jiaodong Penisula and its tectonic implications. Chin. J. Geophys. 58 (9), 3251–3263. in Chinese with English abstract. https://doi.org/10.6038/cjg20150920.

Petricca, P., Carminati, E., Doglioni, C., Riguzzi, F., 2018. Brittle-ductile transition depth versus convergence rate in shallow crustal thrust faults: Considerations on seismogenic volume and impact on seismicity. Phys. Earth Planet. Inter. 284, 72–81. https://doi.org/10.1016/j.pepi.2018.09.002.

Qiu, Y.M., Groves, D.I., McNaughton, N.J., Wang, L.G., Zhou, T.H., 2002. Nature, age, and tectonic setting of granitoid-hosted, orogenic gold deposits of the Jiaodong Peninsula, eastern North China Craton, China. Miner. Depos. 37, 283–305. https://doi.org/10.1007/s00126-001-0238-3.

Seton, M., Müller, R.D., Zahirovic, S., Gaina, C., Torsvik, T., Shephard, G., Talsma, A., Gurnis, M., Turner, M., Maus, S., Chandler, M., 2012. Global continental and ocean basin reconstructions since 200Ma. Earth-Sci. Rev. 113 (3–4), 212–270. https://doi.org/10.1016/j.earscirev.2012.03.002.

Shen, Y.K., Deng, J., Xu, Y.B., 2005. Geological significance of lampropyre during gold mineralization in the Linglong ore field. Geology and prospecting 41 (3), 45–49 (in Chinese with English abstract).

Sobolev, S.V., Babeyko, A.Y., 1994. Modeling of mineralogical composition, density and elastic wave velocities in anhydrous magmatic rocks. Surv. Geophys. 15, 515–544. https://doi.org/10.1007/bf00690173.

Song, M.C., 2015. The main achievements and key theory and methods of deep-seated prospecting in the Jiaodong gold concentration area, Shandong Province. Geological Bulletin of China 34 (9), 1758–1771 (in Chinese with English abstract).

Song, M.C., Li, S.Z., Santosh, M., Zhao, S.J., Shan, Y., Yi, P.H., Cui, S.X., Lu, G.X., Xu, J.X., Song, Y.X., Zhou, M.L., 2015. Types, characteristics and metallogenesis of gold deposits in the Jiaodong Peninsula, Eastern North China Craton. Original. Ore. Geol. Rev. 65, 612–625. https://doi.org/10.1016/j.oregeorev.2014.06.019.

Šumanovac, F., Hegedűs, E., Orešković, J., Kolar, S., Kovács, A.C., Dudjak, D., Kovács, I.J., 2016. Passive seismic experiment and receiver functions analysis to determine crustal structure at the contact of the northern Dinarides and southwestern Pannonian Basin. Geophys. J. Int. 205, 1420–1436. https://doi.org/10.1093/gji/ggw101.

Tang, J., Zheng, Y.F., Wu, Y.B., Gong, B., Liu, X.M., 2007. Geochronology and geochemistry of metamorphic rocks in the Jiaobei terrane: Constraints on its tectonic affinity in the Sulu orogeny. Precambrian Res. 152, 48–82. https://doi.org/10.1016/j.precamres.2006.09.001.

Thompson, A.B., 1999. Some time-space relationships for crustal melting and granitic intrusion at various depths. Geol. Soc. London. Spec. Publ. 168 (1), 7–25. https://doi.org/10.1144/GSL.SP.1999.168.01.02.

Wang, X., Chen, L., Ai, Y.S., Xu, T., Jiang, M.M., Ling, Y., Gao, Y.F., 2018. Crustal structure and deformation beneath eastern and northeastern Tibet revealed by P-wave receiver functions. Earth Planet. Sci. Lett. 497, 69–79. https://doi.org/10.1016/j.epsl.2018.06.007.

Wen, B.J., Fan, H.R., Santosh, M., Hu, F.F., Pirajno, F., Yang, K.F., 2015. Genesis of two different types of gold mineralization in the Linglong gold field, China: Constraints from geology, fluid inclusions and stable isotope. Ore Geol. Rev. 65, 643–658. https://doi.org/10.1016/j.oregeorev.2014.03.018.

Woods, M.T., Davies, G.F., 1982. Late cretaceous genesis of the Kula plate. Earth Planet. Sci. Lett. 58 (2), 161–166. https://doi.org/10.1016/0012-821X(82)90191-1.

Wu, F.Y., Lin, J.Q., Simon, A.W., Zhang, X.O., Yang, J.H., 2005. Nature and significance of the early cretaceous giant igneous event in eastern China. Earth Planet. Sci. Lett. 233, 103–119. https://doi.org/10.1016/j.epsl.2005.02.019.

Wu, F.Y., Xu, Y.G., Gao, S., Zheng, J.P., 2008. Lithospheric thinning and destruction of the North China Craton. Acta Petrol. Sin. 24 (6), 1145–1174 (in Chinese with English abstract).

Xu, Y.G., Li, H.Y., Pang, C.J., He, B., 2009. On the timing and duration of the destruction of the North China Craton. Chin. Sci. Bull. 54. https://doi.org/10.1007/s11434-009-0346-5.

Xu, S., Unsworth, M.J., Hu, X.Y., Mooney, W., 2019. Magnetotelluric evidence for asymmetric simple shear extension and lithospheric thinning in South China. J. Geophys. Res. Solid Earth 124 (1), 104–124. https://doi.org/10.1029/2018JB016505.

Yang, W.C., 2002. Geophysical profiling across the Sulu ultra-high-pressure metamorphic belt, eastern China. Tectonophysics 354 (3), 277–288. https://doi.org/10.1016/S0040-1951(02)00386-4.

Yang, Q.Y., Santosh, M., 2015. Early cretaceous magma flare-up and its implications on gold mineralization in the Jiaodong Peninsula, China. Ore Geol. Rev. 65, 626–642. https://doi.org/10.1016/j.oregeorev.2014.01.004.

Yang, J.H., Wu, F.Y., Wilde, S.A., 2003a. A review of the geodynamic setting of large-scale late Mesozoic gold mineralization in the North China Craton: an association with lithospheric thinning. Ore Geol. Rev. 23, 125–152. https://doi.org/10.1016/S0169-1368(03)00033-7.

Yang, J.H., Chu, M.F., Liu, W., Zhai, M.G., 2003b. Geochemistry and petrogenesis of Guojialing granodiorites from the northwestern Jiaodong Peninsula, eastern China. Acta Petrol. Sin. 19 (4), 692–700.

Yang, J.H., Wu, F.Y., Chung, S.L., Wilde, S.A., Chu, M.F., Lo, C.H., Song, B., 2005. Petrogenesis of early cretaceous instructions in the Sulu ultrahigh-pressure orogenic belt, East China and their relationship to lithospheric thinning. Chem. Geol. 222, 200~231. https://doi.org/10.1016/j.chemgeo.2005.07.006.

Yang, L.Q., Deng, J., Wang, Z.L., Zhang, L., Guo, L.N., Song, M.C., Zheng, X.L., 2014. Mesozoic gold metallogenic system of the Jiaodong gold province, eastern China. Acta Petrol. Sin. 30 (9), 2447–2467 (in Chinese with English abstract).

Yin, A., Nie, S.Y., 1993. An indentation model for the North and South China collision and the development of the Tan-Lu and Honam Fault Systems, eastern Asia. Tectonics 12, 801–813. https://doi.org/10.1029/93TC00313.

Ying, J.F., Zhang, H.F., Tang, Y.J., Su, B.X., Zhou, X.H., 2013. Diverse crustal components in pyroxenite xenoliths from Junan, Sulu orogenic belt: Implications for lithospheric modification invoked by continental subduction. Chem. Geol. 356, 181–192. https://doi.org/10.1016/j.chemgeo.2013.08.006.

Yu, X.F., Shan, W., Xiong, Y.X., Geng, K., Sun, Y.Q., Chi, N.J., Guo, B.K., Li, D.P., Li, H.K., Song, Y.X., Yang, D.P., 2018. Deep structural framework and genetic analysis of gold concentration areas in the northwestern Jiaodong Peninsula, China: a new understanding based on high-resolution reflective seismic survey. Acta Geol. Sin. 92 (5), 1823–1840.

Yuan, X.H., Ni, J., Kind, R., Mechie, J., Sandvol, E., 1997. Lithospheric and upper mantle structure of southern Tibet from a seismological passive source experiment. J. Geophys. Res. 102 (B12), 27491–27500. https://doi.org/10.1029/97JB02379.

Zhai, M.G., Guo, J.H., Wang, Q.C., Ye, K., Cong, B.L., Liu, W.J., 2000. Division of petrological-tectonic units in the Northern Sulu ultra-high pressure zone: an example of thick-skin thrust of crystalline units. Sci. Geol. Sin. 35 (1), 16–26 (in Chinese with English abstract).

Zhang, K.J., 1997. North and South China collision along the eastern and southern North China margins. Tectonophysics 270, 145–156. https://doi.org/10.1016/S0040-1951(96)00208-9.

Zhang, T., Zhang, Y.Q., 2007. Geochronological sequence of Mesozoic intrusive Magmatism in Jiaodong Peninsula and its tectonic constraints. Geol. J. China Univ. 13 (2), 323–336 (in Chinese with English abstract).

Zhang, Y.Q., Dong, S.W., Shi, W., 2003. Cretaceous deformation history of the middle Tan-Lu fault zone in Shandong Province, eastern China. Tectonophysics 363, 243–258. https://doi.org/10.1016/S0040-1951(03)00039-8.

Zhang, Y.Q., Li, J.L., Zhang, T., Yuan, J.Y., 2007. Late Mesozoic kinematic history of the Muping-Jimo fault zone in Jiaodong Peninsula, Shandong Province, East China. Geological Review 53 (3), 289–300.

Zhang, K., Lu, Q.T., Yan, J.Y., Hu, H., Fu, G.M., Shao, L.S., 2018. Crustal structure beneath the Jiaodong Peninsula, North China, revealed with a 3D inversion model of magnetotelluric data. J. Geophys. Eng. 15, 2442–2454. https://doi.org/10.1088/1742-2140/aaca5e.

Zhao, Z.F., Zheng, Y.F., Chen, Y.X., Sun, G.C., 2017. Partial melting of subducted continental crust: Geochemical evidence from synexhumation granite in the Sulu Orogen. Geol. Soc. Am. Bull. 129 (11/12), 1692–1707. https://doi.org/10.1130/B31675.1.

Zheng, Y.F., Zhou, J.B., Wu, Y.B., Xie, Z., 2005. Low-grade metamorphic rocks in the Dabie-Sulu orogenic belt: a passive-margin accretionary wedge deformed during continent subduction. Int. Geol. Rev. 47, 851–871. https://doi.org/10.2747/0020-6814.47.8.851.

Zheng, T.Y., Chen, L., Zhao, L., Xu, W.W., Zhu, R.X., 2006. Crust-mantle structure difference across the gravity gradient zone in North China Craton: Seismic image of the thinned continental crust. Phys. Earth Planet. Inter. 159, 43–58. https://doi.org/10.1016/j.pepi.2006.05.004.

Zheng, T.Y., Zhao, L., Zhu, R.X., 2008a. Insight into the geodynamics of cratonic reactivation from seismic analysis of the crust-mantle boundary. Geophys. Res. Lett. 35, L08303. https://doi.org/10.1029/2008GL033439.

Zheng, T.Y., Zhao, L., Xu, W.W., Zhu, R.X., 2008b. Insight into modification of North China Craton from seismological study in the Shandong Province. Geophys. Res. Lett. 35, L22305. https://doi.org/10.1029/2008GL035661.

Zheng, X.F., Yao, Z.X., Liang, J.H., Zheng, J., 2010. The role played and opportunities provided by IGP DMC of China National Seismic Network in Wenchuan earthquake disaster relief and researches. Bull. Seismol. Soc. Am. 100 (5B), 2866–2872. https://doi.org/10.1785/0120090257.

Zhou, J.B., Wilde, S.A., Zhao, G.C., Zhang, X.Z., Zheng, C.Q., Jin, W., Cheng, H., 2008. SHRIMP U–Pb zircon dating of the Wulian complex: defining the boundary between the North and South China Cratons in the Sulu Orogenic Belt, China. Precambrian Res. 162, 559–576. https://doi.org/10.1016/j.precamres.2007.10.008.

Zhu, L.P., Kanamori, H., 2000. Moho depth variation in southern California from teleseismic receiver functions. J. Geophys. Res. 105 (B2), 2969–2980. https://doi.org/10.1029/1999JB900322.

Zhu, R.X., Zheng, T.Y., 2009. Destruction geodynamics of the North China Craton and its Paleoproterozoic plate tectonics. Chin. Sci. Bull. 54 (14), 1950–1961. in Chinese with English abstract. https://doi.org/10.1007/s11434-009-0451-5.

Zhu, R.X., Chen, L., Wu, F.Y., Liu, J.L., 2011. Timing, scale and mechanism of the destruction of the North China Craton. Sci. China Earth Sci. 54, 789–797. https://doi.org/10.1007/s11430-011-4203-4.

Zhu, R.X., Fan, H.R., Li, J.W., Meng, Q.R., Li, S.R., Zeng, Q.D., 2015. Decratonic gold deposits. Sci. China Earth Sci. 58, 1523–1537. https://doi.org/10.1007/s11430-015-5139-x.

Zhu, R.X., Zhang, H.F., Zhu, G., Meng, Q.R., Fan, H.R., Yang, J.H., Wu, F.Y., Zhang, Z.Y., Zheng, T.Y., 2017. Craton destruction and related resources. Int. J. Earth Sci. 106, 2233–2257. https://doi.org/10.1007/s00531-016-1441-x.

Zhu, G., Liu, C., Gu, C.C., Zhang, S., Li, Y.J., Su, N., Xiao, S.Y., 2018. Oceanic plate subduction history in the western Pacific Ocean: Constraint from late Mesozoic evolution of the Tan-Lu Fault Zone. Sci. China Earth Sci. 61, 386–405. https://doi.org/10.1007/s11430-017-9136-4.